System Identification for Propellers at High Incidence Angles

Benjamin M. Simmons*
NASA Langley Research Center, Hampton, VA, 23681

Propellers used for electric vertical takeoff and landing (eVTOL) aircraft propulsion systems experience a wide range of aerodynamic conditions, including large incidence angles relative to oncoming airflow. In oblique flow, propellers exhibit deviations in thrust and torque oriented along the propeller axis of rotation, as well as significant off-axis forces and moments. Although important for modeling eVTOL aircraft aerodynamics, sparse experimental data or mathematical models exist for propellers at incidence. This paper describes a propulsion system modeling methodology for the LA-8 tandem tilt-wing, eVTOL aircraft. System identification methods are applied to isolated propeller wind tunnel data gathered across the vehicle's flight envelope to develop a mathematical model of the propulsion system, including a static motor model, dynamic motor model, and propeller aerodynamic model. Modeling results validated against data withheld from the modeling process indicate good predictive capability and agree with theoretical expectations. The results are followed by a discussion of model implementation strategies into high-fidelity eVTOL aircraft simulations.

Nomenclature

$C_{T_x}, C_{T_y}, C_{T_z}$	=	propeller force coefficients
$C_{Q_x}, C_{Q_y}, C_{Q_z}$	=	propeller moment coefficients
D	=	propeller diameter, ft
$\hat{e}$	=	normalized residual
i_p	=	propeller incidence angle, rad
J	=	advance ratio
J_x	=	normal advance ratio
J_z	=	tangential advance ratio
n	=	propeller and motor rotational speed, revolutions/s
NMAE	=	normalized mean absolute error
NRMSE	=	normalized root-mean-square error

Presented as Paper 2021-1190 at the AIAA SciTech 2021 Forum, Virtual Event, 11–15 & 19–21 January 2021.
*Research Engineer, Flight Dynamics Branch, MS 308, Member AIAA.

p, q, r	=	vehicle body-axis angular velocity, rad/s
PSE	=	predicted squared error
Q_x, Q_y, Q_z	=	propeller moments, ft-lbf
$\bar{q}$	=	freestream dynamic pressure, lbf/ft^2
R^2	=	coefficient of determination
Re	=	propeller blade Reynolds number
T_x, T_y, T_z	=	propeller forces, lbf
u, v, w	=	vehicle body-axis velocity, ft/s
u_p, v_p, w_p	=	local propeller velocity, ft/s
V	=	freestream airspeed, ft/s
δ_w	=	wing angle, rad
η	=	motor pulse width modulation (PWM) command, μs
μ	=	air dynamic viscosity, lbf-s/ft^2
ρ	=	air density, slug/ft^3
$s(\hat{\theta})$	=	parameter standard error
$\hat{\theta}$	=	parameter estimate
ξ_p	=	local velocity projection angle on the propeller disk plane, rad

I. Introduction

Electric vertical takeoff and landing (eVTOL) aircraft are currently drawing significant interest in the aerospace industry as an enabling technology for future Urban Air Mobility (UAM) transportation missions. Many eVTOL vehicle designs are a hybrid between a fixed-wing and rotary-wing aircraft, which allows both precise low-speed vertical maneuvering and efficient high-speed cruise capabilities. Common eVTOL configurations include tilt-wings, tilt-rotors, and dual propulsion systems, with electrically-driven propellers distributed along the vehicle [1]. Multiple research efforts have been initiated to develop conceptual and tangible eVTOL vehicles to better understand their flight characteristics and develop technology allowing mainstream integration of this new type of aircraft [2–5].

Mission requirements for eVTOL aircraft necessitates operation in a wide variety of flight conditions spanning hover, transition, and forward flight. Consequently, their propellers experience aerodynamic conditions that significantly differ from conventional propeller and rotor operation in a typical flight profile. Propeller aerodynamics are conventionally modeled in the axial airflow condition where data tables or functional representations of axial thrust and torque coefficients are sufficient to model the propeller aerodynamics. However, at high incidence angles, off-axis propulsive forces and moments become significant, and the axial thrust and torque deviate from nominal axial airflow values.

Furthermore, at the time of this writing, limited data and mathematical modeling strategies exist for propellers operating at high incidence angles, which provided motivation for the research investigation described in this paper.

The objective of this work is to identify a model of the motor characteristics and propeller aerodynamics for the Langley Aerodrome No. 8 (LA-8) aircraft [5], as part of the development of a high-fidelity flight dynamics simulation of the vehicle. The LA-8 aircraft, pictured in Fig. 1, is a tandem tilt-wing, eVTOL configuration with four propellers mounted to each rotating wing. The distributed electric propulsion design leads to significant aerodynamic contributions from the airframe, propulsors, and airframe-propulsion interactions. This work describes the model development effort used to characterize the isolated propulsion unit at all incidence angles experienced by the aircraft, and is complimented by other current research pertaining to the LA-8 aircraft [5–12]. The propulsion model identification strategies utilizing wind tunnel testing and novel application of system identification techniques are thoroughly explained and shown to be effective for developing globally-valid high-fidelity propulsion models. Although the information in this paper is presented in the context of the LA-8 vehicle, the proposed propeller model identification strategies can be applied to many other similar eVTOL vehicles currently under development* and future eVTOL vehicles.

(a) LA-8 front view **(b) LA-8 rear view**

Fig. 1 LA-8 mounted in the NASA Langley 12-Foot Low-Speed Tunnel.

This paper is organized as follows. Section II presents pertinent background on propeller aerodynamics theory and previous research for propellers operating at high incidence angles. Section III describes the wind tunnel testing effort. Section IV gives an overview of the system identification methods employed and outlines the overall propulsion modeling approach. The motor modeling results are given in Sec. V and propeller aerodynamic modeling results are given in Sec. VI. Practical vehicle simulation implementation strategies are highlighted in Sec. VII and overall conclusions are summarized in Sec. VIII.

*Information available online at https://evtol.news/aircraft [accessed November 2020]

II. Background

This section provides a theoretical background on axial propeller aerodynamics and propeller aerodynamics at incidence. Related research efforts in high incidence angle propeller aerodynamics are also summarized. Understanding of this background information is essential for postulating propeller modeling strategies as well as interpretation of the results presented.

A. Axial Propeller Aerodynamics

Propeller aerodynamics are well-defined and well-researched for nominal operating conditions in axial flow where aerodynamic predictions can be made analytically and/or experimentally. Theoretical techniques include momentum theory, blade element methods, and vortex theories [13]. Experimental techniques typically consist of developing data tables or functional representations from wind tunnel data. For propellers in airflow normal to the propeller disk, the propeller only produces a net thrust force and a net aerodynamic torque acting along the axis of rotation [14]. The individual propeller blades can be thought of as rotating wings which each produce a lift force perpendicular to the relative flow direction and a drag force parallel to the relative flow direction [15]. The summed lift forces produced by the propeller blades is the propeller thrust T_x. The summed drag forces results in a net moment about the propeller shaft opposite to the direction of rotation, which is the propeller aerodynamic torque Q_x.

Propeller data are generally presented as a representation of thrust coefficient C_{T_x} and torque coefficient C_{Q_x} (or equivalently by power coefficient $C_P = 2\pi C_{Q_x}$ where $P = 2\pi n Q_x$). The thrust and torque coefficients are defined as

$$C_{T_x} = \frac{T_x}{\rho n^2 D^4} \tag{1}$$

$$C_{Q_x} = \frac{Q_x}{\rho n^2 D^5} \tag{2}$$

where n is the propeller rotational speed in revolutions per second, ρ is the air density, and D is the propeller diameter. The thrust and torque coefficients can be shown through dimensional analysis to be a function of advance ratio J, propeller blade Reynolds number Re, and propeller tip Mach number M_{tip} for a given propeller design [14, 16]. Because propeller similitude relations to scale propeller aerodynamics are limited [17], due to differences in boundary layer characteristics [18], propeller characteristics must be tested at full-scale to properly capture the advance ratio, Reynolds number, and Mach number effects.

Advance ratio J, which relates to the linear distance traveled by the propeller in one revolution, is defined as

$$J = \frac{V}{nD} \tag{3}$$

where V is the freestream velocity and other variables follow their earlier definition. Advance ratio generally has the

largest effect on propeller aerodynamics, and thus, thrust and torque coefficient representations are commonly expressed as only a function of advance ratio. Representing propeller aerodynamics only as a function of advance ratio requires that airflow is parallel to the propeller axis of rotation as well as the assumptions that viscous and compressibility effects are negligible [14].

Reynolds number is a dimensionless quantity which corresponds to the ratio of inertial to viscous forces acting on a body. For full-scale aircraft propellers, the propeller blade Reynolds number effects are minimal and can generally be neglected. For subscale propellers, the Reynolds number is lower, indicating that the viscous forces become important. This effect is manifested as a thicker boundary layer, which is more likely to result in flow separated from the propeller surface [18] and results in propeller performance degrading at lower Reynolds number [19, 20]. The equation used herein for the propeller blade Reynolds number Re follows the definition given in Ref. [20],

$$Re = \frac{\rho V_p c}{\mu} \tag{4}$$

where ρ is air density, c is the propeller chord at 75% blade length, μ is the dynamic viscosity, and $V_p = 0.75\pi nD$ is the propeller blade linear speed at 75% blade length.

Mach number is the ratio of flow speed to the speed of sound, which physically represents the ratio of inertial forces to forces related to compressibility of the fluid [18]. For subscale UAVs, the propeller tip Mach number generally remains low enough ($M_{tip} < 0.3$) such that compressibility effects can be ignored, which is the approach taken in this work.

B. Propeller Aerodynamics at Nonzero Incidence Angle

When the airflow relative to a propeller is not parallel to the axis of rotation, the propeller will produce auxiliary forces and moments other than the axial thrust and torque [14]. In this condition, periodic variation in propeller blade local angle of attack results in a non-uniform load distribution on the propeller disk. Thus, in a general case of arbitrary flow direction relative to the propeller disk, propeller forces and moments will also be dependent on angle between the freestream velocity and propeller axis of rotation, in addition to advance ratio, propeller blade Reynolds number, tip Mach number, and the propeller design. This angle between the freestream airflow and propeller rotation axis is referred to in this work as the *propeller incidence angle*, i_p, shown in Fig. 2. The value of i_p is zero when airflow is normal to the propeller disk, opposing the direction of axial thrust.

One additional auxiliary force and one additional auxiliary moment are predicted theoretically from the periodic lift and drag imbalance on the individual propeller blades [14, 15]. To explain these phenomena, it is useful to consider a common example of a front mounted propeller on an airplane in level, forward flight at positive angle of attack, where it is assumed that the propeller axis of rotation coincides with the x body-axis of the airplane. The propeller blades

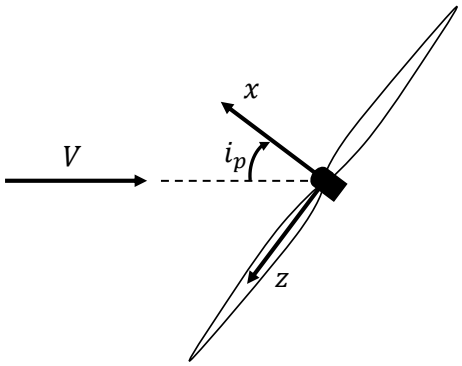

Fig. 2 Propeller incidence angle definition and coordinate system.

moving downward will produce more lift than the propeller blades moving upward because the downward moving blade is experiencing a higher angle of attack and relative airspeed. Consequently, the net center of thrust force is offset from the propeller axis of rotation, favoring the side of downward blade movement. When the net thrust force is transferred to the center of the propeller, a net yawing moment is observed acting to rotate the downward moving propeller blades into the oncoming airflow. This effect is often referred to as the p-factor. The individual propeller blade drag forces are also larger on the side of downward movement, again due to the greater relative angle of attack and airspeed, resulting in a net normal force directed upward for the current example. Thus, a propeller on an airplane at positive angle of attack will produce a normal force and a yawing moment in addition to the conventional axial thrust and torque. Following similar reasoning, the example propeller in sideslip will instead produce pitching moment and side force as the auxiliary force and moment.

An analytical treatment of airplane propeller aerodynamics at low angle of attack presented in Ref. [15] agrees with the qualitative conclusions obtained from the preceding example. For a propeller operating at a small nonzero angle of attack and zero sideslip, the normal force and yawing moment are shown to be linearly proportional to the propeller incidence angle; pitching moment and side force coefficients are theoretically zero. It is also shown that for low incidence angle conditions, small perturbations in incidence angle have no effect on axial thrust and torque.

The propeller side force T_y, normal force T_z, pitching moment Q_y, and yawing moment Q_z can be non-dimensionalized in a manner similar to the thrust T_x and torque Q_x [15]. The propeller normal force coefficient C_{T_z}, side force coefficient C_{T_y}, pitching moment coefficient C_{Q_y}, and yawing moment coefficients C_{Q_z}, are defined as:

$$C_{T_y} = \frac{T_y}{\rho n^2 D^4},\ C_{T_z} = \frac{T_z}{\rho n^2 D^4},\ C_{Q_y} = \frac{Q_y}{\rho n^2 D^5},\ C_{Q_z} = \frac{Q_z}{\rho n^2 D^5} \tag{5}$$

The propeller force and moment sign convention used in this work follows the right-handed propeller coordinate system shown in Fig. 2, where the y-axis is pointed into the page.

Several works have employed methods for theoretically and computationally capturing propeller aerodynamics at

incidence [15, 21–28], however, experimental techniques provide the most accuracy in revealing the highly complex and nonlinear behavior of high incidence angle propeller aerodynamics. Early experiments described in Refs. [29, 30] were conducted for propellers with varying incidence angle as well as flow speed, blade angle, and rotational speed. These works showed similar trends in propeller force and moment variation with incidence angle and demonstrated the effectiveness of using the normal component of advance ratio, $J \cos i_p$, for describing propeller aerodynamics at incidence. Reference [31] extended this work by studying the high incidence angle aerodynamics of isolated propellers as well as propeller-wing interactions, noting aerodynamic differences due to the presence of the wing.

The increased interest in efficient jet propulsion subsequent to the above work resulted in propeller aerodynamics research becoming dormant for several decades, until recently when increased interest in electrically-powered unmanned aerial vehicles, distributed electric propulsion, and eVTOL designs arose in the aerospace community. In Ref. [32], wind tunnel testing of a subscale propeller at incidence angles ranging from 0° to 180° with flow speeds up to 29.5 ft/s was conducted. Normal force magnitude was found to be smaller than axial thrust but still significant at nonzero incidence angles; side force was found to be negligible for all incidence angles. Off-axis pitching and yawing moments were found to be comparable in magnitude to the aerodynamic torque along the axis of rotation at high incidence angles. Notably, this pitching moment result is not predicted by the propeller theory described in Ref. [15] showing the limitations of the analytical treatment of propellers at incidence. The significant pitching moment at high incidence angles can be attributed to non-uniform airflow through the front and rear portions of the propeller relative to the airflow, which leads to a tendency for the propeller to pitch upward at near 90° incidence angles [32]. Reference [33] followed this work by testing the same propeller and performed additional testing on multiple 3D printed propeller blades. The measured propeller force and moment coefficients showed reasonable agreement between the two testing efforts.

III. Wind Tunnel Experimentation

An isolated propeller wind tunnel experiment was performed in the NASA Langley Research Center 12-Foot Low-Speed Tunnel[†] to facilitate development of a high-fidelity propulsion system model for the LA-8 aircraft. The test was designed to cover the operational envelope of the LA-8 aircraft and match the propeller flight conditions experienced in a previous LA-8 wind tunnel entry used to develop an aerodynamic model of the aircraft [8, 9]. The testing effort is described in detail in Ref. [34] and is summarized here.

The propellers tested for this study were folding, fixed-pitch, three-bladed, 16-inch diameter, 8-inch pitch, clockwise and counterclockwise rotating propellers used on the LA-8 aircraft. Figure 3 shows photographs of the propeller blade planform, and the assembled three-bladed propeller. The propellers were powered by a 450 KV electric motor and 100 amp electronic speed control (ESC). The clockwise rotating propellers, as viewed from behind the aircraft, are commercially available, whereas the counterclockwise propellers were custom produced. While the custom

[†]Information available online at https://researchdirectorate.larc.nasa.gov/12-foot-low-speed-tunnel-12-ft-lst/ [accessed November 2020]

counterclockwise propellers were intended to mirror the clockwise propeller geometry and aerodynamics, slight differences in the propeller characteristics were noted through physical examination and were reflected in test results [34].

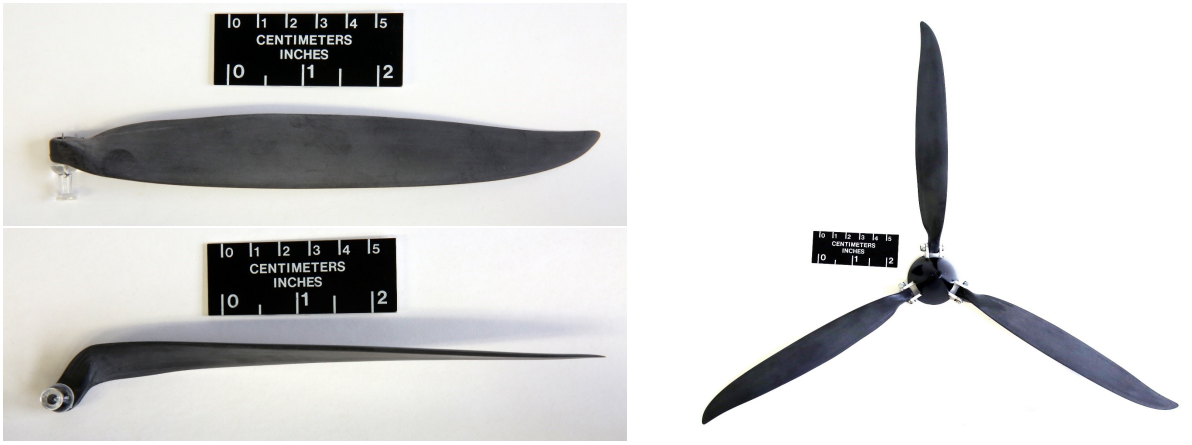

(a) Propeller blade (top and side view) **(b) Assembled three bladed propeller (front view)**

Fig. 3 LA-8 experimental propeller.

Static wind tunnel testing for each propeller variant was conducted in a one-factor-at-a-time manner varying dynamic pressure $\bar{q}$, motor PWM command η, and incidence angle i_p. At each test point, the six force and moment components were measured using a strain gauge balance and a propeller rotational speed measurement was provided by the ESC. Each individual wind tunnel run was executed by sweeping incidence angle from 0° to a maximum value defined for each dynamic pressure setting (between 60° to 180°), while holding a constant dynamic pressure and motor pulse width modulation (PWM) command throughout the run. This procedure is reflected in the multi-exposure image of a test run depicted in Fig. 4a. The propeller coordinate system and incidence angle measurement is depicted in Fig. 4b. Testing was performed at dynamic pressures ranging from 0 to 6 psf, which corresponds to a freestream airspeed from 0 to 71 ft/s at standard sea level conditions. Motor PWM signal inputs were varied evenly at five different settings between 1350 to 1600 μs for all dynamic pressures and incidence angles, which translates to a propeller rotational speed range of approximately 1500 to 6000 RPM. The designed test points are shown graphically in Fig. 5 in terms of freestream airflow and incidence angle.

While the test point conditions were specified using dynamic pressure and motor PWM command, these settings were used to indirectly sweep variables more pertinent to propeller aerodynamics: freestream airspeed and propeller rotational speed. These latter quantities were then further reduced to calculate propeller advance ratio (Eq. (3)) and propeller blade Reynolds number (Eq. (4)). Changes in dynamic pressure change the flow velocity, which drives changes in propeller advance ratio. Changes in motor PWM command change the propeller rotational speed, which has the primary effect of changing the Reynolds number experienced by the propeller blades, but also contributes to changes in the propeller advance ratio.

(a) Multi-exposure image of a propeller wind tunnel run **(b) Propeller test coordinate system**

Fig. 4 LA-8 propeller mounted in the NASA Langley 12-Foot Low-Speed Tunnel.

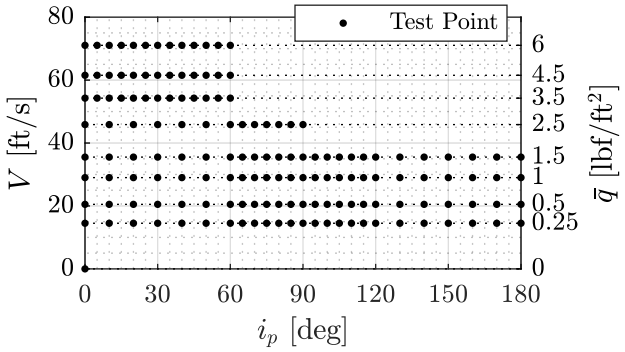

Fig. 5 Designed propeller wind tunnel test points for freestream velocity and incidence angle.

In addition to the nominal static test matrix for each propeller displayed in Fig. 5, several repeat and validation-specific runs were made to ensure data quality and allow testing of the model predictive capability. Validation runs were taken with different motor speed and dynamic pressure settings within the ranges tested. Furthermore, several continuous data collection runs containing variable amplitude motor step inputs were made at multiple dynamic pressure settings with $0^\circ \leq i_p \leq 60^\circ$ to aid development of a motor dynamics model.

IV. Model Identification Methodology

The next sections give an overview of the methods used to identify models for the LA-8 propulsion system, including model structure identification, parameter estimation, and model validation. A comprehensive description of these techniques, among other system identification methods, is given in Ref. [35]. The model structure identification and parameter estimation methods used in this work were adapted from the System IDentification Programs for AirCraft (SIDPAC) software toolbox.[‡] SIDPAC consists of a collection of amendable MATLAB® scripts that can be tailored for a particular modeling effort. This flexibility was beneficial for refinement of novel propeller model development

[‡]Information available online at https://software.nasa.gov/software/LAR-16100-1 [accessed November 2020]

strategies.

A. Least-Squares Parameter Estimation

Ordinary least-squares regression is used to estimate a vector of n_p unknown model parameters in a vector $\boldsymbol{\theta}$ for a given model $\boldsymbol{y} = \boldsymbol{X\theta}$ [35]. Here $\boldsymbol{y}$ is the length N model response vector and $\boldsymbol{X}$ is a $N \times n_p$ matrix consisting of column vectors of regressors assumed to be measured without error. The regression equation, including a measurement of the response variable $\boldsymbol{z}$, corrupted by constant variance, zero-mean, and uncorrelated measurement error $\boldsymbol{\nu}$, is given as:

$$\boldsymbol{z} = \boldsymbol{X\theta} + \boldsymbol{\nu} \tag{6}$$

For least-squares parameter estimation, the optimal estimate of the unknown parameters $\boldsymbol{\theta}$ is determined by minimizing the cost function:

$$J(\boldsymbol{\theta}) = \frac{1}{2} \left(\boldsymbol{z} - \boldsymbol{X\theta}\right)^T \left(\boldsymbol{z} - \boldsymbol{X\theta}\right) \tag{7}$$

It follows that the solution to compute an optimal estimate of the unknown parameters is

$$\hat{\boldsymbol{\theta}} = \left(\boldsymbol{X}^T \boldsymbol{X}\right)^{-1} \boldsymbol{X}^T \boldsymbol{z} \tag{8}$$

where $\hat{\boldsymbol{\theta}}$ is a vector of n_p estimated parameters. Assuming uncorrelated measurement errors and an adequate model structure is used to compute a modeled response variable history $\hat{\boldsymbol{y}} = \boldsymbol{X}\hat{\boldsymbol{\theta}}$, a length n_p vector of standard errors $\boldsymbol{s}(\hat{\boldsymbol{\theta}})$ corresponding to the estimated parameters $\hat{\boldsymbol{\theta}}$ is given as:

$$\boldsymbol{s}(\hat{\boldsymbol{\theta}}) = \sqrt{\left(\frac{\left(\boldsymbol{z} - \hat{\boldsymbol{y}}\right)^T \left(\boldsymbol{z} - \hat{\boldsymbol{y}}\right)}{N - n_p}\right) \text{diag} \left[\left(\boldsymbol{X}^T \boldsymbol{X}\right)^{-1}\right]} \tag{9}$$

The least-squares regression method yields a simple parameter estimation solution, but a method of determining an adequate model structure is still required to obtain a quality model.

B. Model Structure Determination

Selecting a suitable model structure is a challenging aspect of the present work due to the lack of past research in model development for propellers at incidence. The explanatory variables, the expected model terms, and overall model form were unknown at the onset of this work. To facilitate rapid examination of multiple different modeling strategies, an automated technique to develop a model structure was desired while still developing a quality parsimonious model structure. Multivariate orthogonal function (MOF) modeling, described in Refs. [35, 36], meets these specifications, and thus, was selected as the model structure identification technique for this work. MOF has been successfully used

in previous wind tunnel database development studies to identify nonlinear polynomial models describing aircraft aerodynamics in a large range of flight conditions [37, 38].

The MOF modeling approach is initiated by orthogonalizing a predefined set of candidate regressors using an algorithm such as Gram-Schmidt orthogonalization or QR decomposition. Orthogonal regressors are convenient for model structure development because of the ability to independently assess the candidate regressors potential to model the response variable—this facilitates only including model terms that significantly contribute to model effectiveness. Upon orthogonalization of candidate regressors, the least-squares regression equation can be reformulated as

$$\boldsymbol{z} = \boldsymbol{P}\boldsymbol{a} + \boldsymbol{\nu} \tag{10}$$

where $\boldsymbol{P}$ is a $N \times n_p$ matrix consisting of column vectors holding orthogonal regressors $\boldsymbol{p}_i$ from $i = 1, 2, ..., n_p$, and $\boldsymbol{a}$ is a vector of n_p unknown parameters. The least squares cost function becomes

$$J(\boldsymbol{a}) = \frac{1}{2}(\boldsymbol{z} - \boldsymbol{P}\boldsymbol{a})^T (\boldsymbol{z} - \boldsymbol{P}\boldsymbol{a}) \tag{11}$$

following Eq. (7). Similarly, the least-squares solution and uncertainty estimates emulate the form of Eq. (8) and Eq. (9) by substituting in the orthogonal regressor matrix $\boldsymbol{P}$ with parameter estimates $\hat{\boldsymbol{a}}$. Because the matrix $\boldsymbol{P}^T\boldsymbol{P}$ is diagonal due to the mutual orthogonality of the regressors, the least-squares estimate for the i^{th} parameter decouples and takes the form

$$\hat{a}_i = \frac{\boldsymbol{p}_i^T \boldsymbol{z}}{\boldsymbol{p}_i^T \boldsymbol{p}_i} \tag{12}$$

to obtain a vector of estimated parameters, $\hat{\boldsymbol{a}} = \left[\hat{a}_1, \hat{a}_2, ..., \hat{a}_{n_p}\right]^T$. It follows that the least-squares cost function can be rewritten as

$$J(\hat{\boldsymbol{a}}) = \frac{1}{2}\left(\boldsymbol{z}^T\boldsymbol{z} - \sum_{i=1}^{n_p} \frac{\left(\boldsymbol{p}_i^T \boldsymbol{z}\right)^2}{\boldsymbol{p}_i^T \boldsymbol{p}_i}\right) \tag{13}$$

which highlights the fact that the contribution of each orthogonal regressor to improve the least-squares model fit can be assessed independently from other orthogonal regressors in a particular model structure. This allows a model structure to be identified without iteration [35].

Using the above developments, the regressors are ranked from highest to lowest decrease in the mean squared fit error (MSFE), which is reflected by the $\left(\boldsymbol{p}_i^T \boldsymbol{z}\right)^2 / \boldsymbol{p}_i^T \boldsymbol{p}_i$ term for each regressor in Eq. (13). In other words, this ranks the regressors from highest to lowest ability to improve the model. Candidate regressors are brought into the model structure in this order. Deciding which terms to include in the final model can then be done in consultation with one or more statistical metrics. The most common threshold for MOF modeling is to minimize the predicted squared error (PSE) [35, 39]. The PSE is the sum of the MSFE for a model and a complexity penalty term related to the number of

terms included in the model:

$$\text{PSE} = \frac{1}{N}\left(\boldsymbol{z} - \boldsymbol{P}\hat{\boldsymbol{a}}\right)^T \left(\boldsymbol{z} - \boldsymbol{P}\hat{\boldsymbol{a}}\right) + \sigma_{max}^2 \frac{p}{N} \tag{14}$$

where p is the number of terms in the current model structure and σ_{max}^2 is an estimate of the upper-bound of mean squared error for the model prediction of data not used to develop the model. The quantity σ_{max}^2 can be estimated using the variance of measured responses between repeated data points or from the variance between the measured response and mean response. The latter is adopted for this work because an insufficient number of repeat points were available to obtain a good estimate of the measurement error variance. When the orthogonalized regressors are ranked as stated above, the PSE metric is guaranteed to have a single global minimum [35].

Another statistical metric that has been used as a stopping criterion for MOF modeling is the coefficient of determination R^2 [40, 41]. The R^2 metric quantifies the model fit by characterizing the amount of variation of the response variable about its mean that is described by the model. Using the orthogonal regressors, the R^2 metric is calculated as:

$$R^2 = \frac{\hat{\boldsymbol{a}}^T \boldsymbol{P}^T \boldsymbol{z} - N\bar{z}^2}{\boldsymbol{z}^T \boldsymbol{z} - N\bar{z}^2} \tag{15}$$

The R^2 metric will always increase with addition of new orthogonalized model terms. Consequently, it is important that each model term added on the basis of the R^2 metric significantly increases its value. A common R^2 increase constituting a significant increase with addition of a new model term is $\Delta R^2 = 0.5\%$ [35]. This means that the model term describes a minimum of 0.5% of the total variation about the mean response.

Both PSE and R^2 were used as a cutoff threshold for candidate model terms to include in the final model structure. After the orthogonal regressors were ranked by their ability to reduce the MSFE, the cutoff for model term addition was chosen to be either the candidate model term that minimized the PSE or the last term to increase R^2 by 0.5%, whichever admitted more terms into the model. This selection was made because in certain circumstances, PSE minimization was found to admit too few terms into the model due to having a rough estimated value of σ_{max}^2. After determining the model terms to include in the model structure, the final parameter values were estimated using least-squares regression in ordinary regressor space. The MOF modeling process used for model structure determination is summarized in Fig. 6.

C. Output-Error Parameter Estimation

While static propulsion models will be shown to be sufficiently identified using the preceding techniques, development of a lower-order representation of the motor dynamics was found to be best solved using output-error parameter estimation. The output-error method estimates unknown parameters in a deterministic dynamic system by minimizing the error between predicted and measured output values using an iterative optimization approach [35, 42]. The following overview

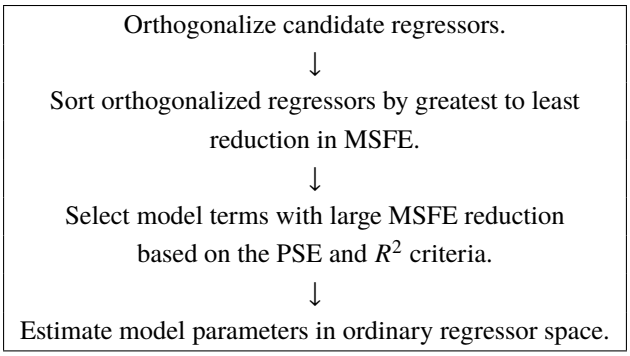

Fig. 6 Summary of the MOF modeling process used for model structure determination.

of the output-error method is presented considering the deterministic nonlinear dynamic system:

$$\dot{\boldsymbol{x}} = \boldsymbol{f}\left(\boldsymbol{x}(t), \boldsymbol{u}(t), \boldsymbol{\theta}\right), \quad \boldsymbol{x}(0) = \boldsymbol{x}_0 \tag{16}$$

$$\boldsymbol{y} = \boldsymbol{g}\left(\boldsymbol{x}(t), \boldsymbol{u}(t), \boldsymbol{\theta}\right) \tag{17}$$

where the state equations $\boldsymbol{f}$ and output equations $\boldsymbol{g}$ can be nonlinear functions of states $\boldsymbol{x}(t)$, inputs $\boldsymbol{u}(t)$, and unknown parameters $\boldsymbol{\theta}$, subject to initial states $\boldsymbol{x}_0$. The N discrete measurements of the dynamic system are

$$\boldsymbol{z}(k) = \boldsymbol{y}(k) + \boldsymbol{\nu}(k), \quad k = 1, 2, ..., N \tag{18}$$

where the system output $\boldsymbol{y}$ is corrupted by zero-mean, Gaussian, white measurement noise $\boldsymbol{\nu}$ with measurement noise covariance $\boldsymbol{R}$.

To minimize the output-error between the measured output $\boldsymbol{z}$ and modeled output $\boldsymbol{y}$, the output-error cost function $J(\boldsymbol{\theta})$ is formulated as

$$J(\boldsymbol{\theta}) = \frac{1}{2}\sum_{k=1}^{N}\left[\boldsymbol{z}(k) - \boldsymbol{y}(k)\right]^T \hat{\boldsymbol{R}}^{-1}\left[\boldsymbol{z}(k) - \boldsymbol{y}(k)\right] \tag{19}$$

for a given estimate of the measurement noise covariance $\hat{\boldsymbol{R}}$ [35]. The $\hat{\boldsymbol{R}}$ matrix, which essentially weights each output based on noise level and signal units, is estimated as:

$$\hat{\boldsymbol{R}} = \frac{1}{N}\sum_{k=1}^{N}\left[\boldsymbol{z}(k) - \boldsymbol{y}(k)\right]\left[\boldsymbol{z}(k) - \boldsymbol{y}(k)\right]^T \tag{20}$$

Minimization of $J(\boldsymbol{\theta})$ constitutes a nonlinear optimization problem that can be approached using the modified Newton-Raphson (Gauss-Newton) method. Optimization proceeds by computing the cost function gradient and Hessian

estimate:

$$\frac{\partial J}{\partial \boldsymbol{\theta}} = -\sum_{k=1}^{N} \left[\frac{\partial \boldsymbol{y}(k)}{\partial \boldsymbol{\theta}}\right]^T \hat{\boldsymbol{R}}^{-1} \left[\boldsymbol{z}(k) - \boldsymbol{y}(k)\right] \tag{21}$$

$$\frac{\partial^2 J}{\partial \boldsymbol{\theta}^2} \approx \sum_{k=1}^{N} \left[\frac{\partial \boldsymbol{y}(k)}{\partial \boldsymbol{\theta}}\right]^T \hat{\boldsymbol{R}}^{-1} \left[\frac{\partial \boldsymbol{y}(k)}{\partial \boldsymbol{\theta}}\right] \tag{22}$$

The estimated parameters $\hat{\boldsymbol{\theta}}$ at each j^{th} iteration are then updated by

$$\Delta\hat{\boldsymbol{\theta}} = -\left[\left(\frac{\partial^2 J}{\partial \boldsymbol{\theta}^2}\right)_j\right]^{-1} \left(\frac{\partial J}{\partial \boldsymbol{\theta}}\right)_j \tag{23}$$

where the new parameter estimates are $\hat{\boldsymbol{\theta}}_{j+1} = \hat{\boldsymbol{\theta}}_j + \Delta\hat{\boldsymbol{\theta}}$. A more detailed description of this output-error method algorithm is presented in Ref. [35].

D. Model Validation

Model validation is an examination of the predictive capability of an identified model using data withheld from the model development process. Validation assessment is performed by comparing the measured response from validation data to the response predicted by the model for equivalent inputs. Additional analysis is performed by analyzing the prediction residuals between the measured and predicted response, $\boldsymbol{e} = \boldsymbol{z} - \hat{\boldsymbol{y}}$. It is useful to compare modeling and prediction residuals because a significant increase in the spread of prediction residuals compared to modeling residuals is a way of diagnosing a poor model fit. Furthermore, statistics of the validation residuals can be computed including the root-mean-square modeling error (RMSE) and mean absolute error (MAE). Both RMSE and MAE were used in this work to assess model performance because of differing assumptions and implications underlying the use of each metric [43].

Residual analysis can be given further interpretability by normalization. The error normalization metric used in this work is the range of response variable measurements used to develop the model, $\text{range}(z) = z_{max} - z_{min}$. Range normalization, opposed to other normalization metrics such as the mean or maximum absolute value of the response variable, provides the fairest comparison between prediction error metrics for this work because axial propeller responses are generally biased above or below zero and off-axis propeller responses are centered about zero. The normalized residual vector is defined as

$$\hat{\boldsymbol{e}} = \frac{\boldsymbol{z} - \hat{\boldsymbol{y}}}{\text{range}(\boldsymbol{z})} \tag{24}$$

Similarly, the normalized root-mean-square modeling error (NRMSE) and normalized mean absolute error (NMAE),

expressed as a percentage, are computed as

$$\text{NRMSE} = 100 \times \frac{1}{\text{range}(z)} \sqrt{\frac{(z-\hat{y})^T (z-\hat{y})}{N}} \tag{25}$$

$$\text{NMAE} = 100 \times \frac{1}{\text{range}(z)} \frac{1}{N} \sum_{i=1}^{N} |z(i) - \hat{y}(i)| \tag{26}$$

E. Modeling Approach Overview

Development of the propulsion model for the LA-8 aircraft is described in the subsequent sections using the preceding system identification techniques. The model is composed of three parts: (1) a static motor model relating PWM throttle command to output propeller speed, (2) a dynamic motor model quantifying the dynamic response of propeller speed from a change in commanded throttle, and (3) a propeller aerodynamic model relating the propeller states to output propulsive forces and moments. The static motor model and propeller aerodynamic model were identified using MOF modeling and least-squares regression. The motor dynamics model was identified using the output-error method. As described in Sec. II, propellers at incidence exhibit more aerodynamic complexity compared to propellers operating in axial airflow, but lack previous research in mathematical model development. Only the final modeling approaches are presented, although several other techniques and variable choices were evaluated by trial-and-error throughout this study to characterize modeling best practices for propellers at incidence. Separate models for the clockwise and counterclockwise rotating LA-8 propellers were developed due to the aforementioned differences in propeller characteristics but, for brevity, modeling results are only presented for the clockwise propeller. Assuming the clockwise and counterclockwise rotating propellers had perfectly mirrored designs, only one orientation would need to be tested—the motor models would be identical and the signs of the lateral propeller force and moment components, Q_x, T_y, and Q_z, would be reversed to model the other propeller.

V. Motor Model Identification

A model of the steady-state and dynamic characteristics of the motor and ESC are needed to relate throttle input signal to motor rotational speed. This relationship is important because throttle input is usually the propulsion command from a control system, whereas motor rotational speed is identical to the propeller rotational speed needed to describe propeller aerodynamics. The objective of this effort is to develop a model to support accurate flight dynamics simulations, so motor electrical characteristics (e.g. see Refs. [44, 45]) are represented by lower-order mathematical descriptions.

A. Static Motor Model

A static motor model describes the steady-state relationship between input motor PWM command η and output motor speed n. This relationship is also affected by freestream velocity V, incidence angle i_p, and propeller geometry.[§] Thus, the explanatory variables are defined in terms of η, V, and i_p for each propeller rotation direction, with the response variable being the motor speed n. Observations during testing showed different static motor behavior for $0^\circ \leq i_p \leq 90^\circ$ and $90^\circ \leq i_p \leq 180^\circ$, resulting from the oncoming airflow either resisting or favoring propeller motion [34]. Between 0° to 90° of incidence, the output rotational speed appeared to be dependent on the normal component of freestream velocity relative to the propeller, $V_x = V \cos i_p$. Between 90° to 180° of incidence, freestream velocity appeared to have little effect on output motor speed.

To incorporate these observations and develop a globally valid model, the explanatory variables used to develop the model structure were throttle command η and the normal component of freestream V_x. Further, η is centered on a reference value of 1475 μs to decorrelate from the constant model parameter and align with the assumptions of a multivariate Taylor series expansion taken from a single reference point [35]. To aid the description of the observed dependence on V_x, the variable was defined in terms of a polynomial spline [46], enacted on the interval $0^\circ \leq i_p \leq 90^\circ$. Thus, the explanatory variables are summarized as

$$\hat{\eta} = \eta - 1475$$

$$V_{x^+} = \begin{cases} V \cos i_p & 0^\circ \leq i_p \leq 90^\circ \\ 0 & 90^\circ < i_p \leq 180^\circ \end{cases}$$

The MOF modeling algorithm described in Sec. IV.B was used to develop the model structure for the static motor models. The identified static motor model equation associated with the clockwise rotating propeller is

$$n = n_o + n_{\hat{\eta}}\hat{\eta} + n_{V_{x^+}^3} V_{x^+}^3 + n_{\hat{\eta}V_{x^+}^2}\hat{\eta}V_{x^+}^2 + n_{\hat{\eta}^2 V_{x^+}^2}\hat{\eta}^2 V_{x^+}^2 + n_{\hat{\eta}^2}\hat{\eta}^2$$

where $\hat{\eta}$ has units of μs, V_{x^+} has units of ft/s, and n has units of revolutions/s. The values for the numerical parameters and uncertainties estimated using least-squares regression are shown in Table 1. The response surface model is plotted in Fig. 7a along with the measured modeling and validation wind tunnel data. The corresponding modeling and validation residuals are shown in Fig. 7b. The low parameter uncertainty and close visual model fit suggest a suitable static motor model has been identified. Modeling and validation metrics for the model are shown in Table 2. The high R^2 value, low modeling NRMSE, and low modeling NMAE values also indicate a good model fit. The low validation NRMSE and NMAE metric values with similar magnitude to the corresponding modeling metrics indicate that the model has good

[§] Advance ratio and Reynolds number are avoided because their definitions involve motor/propeller speed n, the response variable in this case.

prediction capability. It is worthy to note that motor speed may also be a function of certain nuisance factors, such as motor temperature, however, the modeling results indicate that the significant effects were captured by the explanatory variables used in the model.

Table 1 Clockwise static motor model parameter estimates

Parameter	$\hat{\theta}$	$s(\hat{\theta})$	% Error
n_o	$+6.40 \times 10^{+1}$	8.65×10^{-2}	0.14
$n_{\hat{\eta}}$	$+2.72 \times 10^{-1}$	6.66×10^{-4}	0.25
$n_{V_{x^+}^3}$	$+3.45 \times 10^{-5}$	9.30×10^{-7}	2.69
$n_{\hat{\eta} V_{x^+}^2}$	-3.02×10^{-5}	4.29×10^{-7}	1.42
$n_{\hat{\eta}^2 V_{x^+}^2}$	$+1.89 \times 10^{-7}$	5.66×10^{-9}	2.99
$n_{\hat{\eta}^2}$	-2.93×10^{-4}	8.95×10^{-6}	3.05

Table 2 Clockwise static motor model modeling and validation metrics (expressed as a percentage)

R^2	Modeling NRMSE	Modeling NMAE	Validation NRMSE	Validation NMAE
99.6	1.72	1.33	1.46	1.12

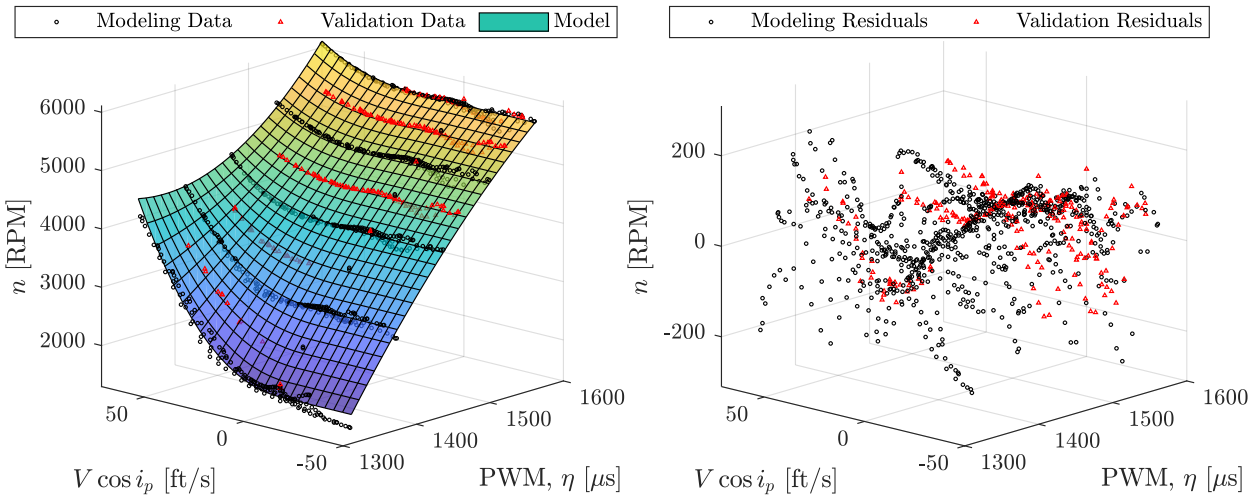

(a) Model response compared to modeling and validation data **(b) Modeling and validation residuals**

Fig. 7 Clockwise static motor model response surface and residuals.

B. Dynamic Motor Model

The dynamic motor model characterizes the dynamic response of actual propeller speed to input motor speed command. The motor speed command is the output of the static motor model described in the previous section. Output-error parameter estimation was performed to identify the model parameters using continuously sampled data

with variable amplitude step commands sent to the propeller over the range of motor PWM signals tested. Testing was conducted at several different airspeed and incidence angle conditions. Dynamic propeller speed measurements did not provide sufficient bandwidth for estimation, so the axial thrust measurement sampled at 2500 Hz was used to identify the motor dynamics. Prior to developing a model, the data were smoothed using a global optimal Fourier smoother [47] and subsequently down-sampled to 100 Hz. Figure 8 shows a sample data set used for estimation. The figure shows that the unfiltered data are very noisy, but the smoothed data reveal the deterministic measurement of interest because the dominant vibrations occur at high frequencies on the order of the propeller rotational speed. Similar noise levels have been seen in previous propeller wind tunnel tests resulting from strong periodic forces attributed to slight propeller imbalances and cyclic, nonuniform flow conditions [32, 48, 49].

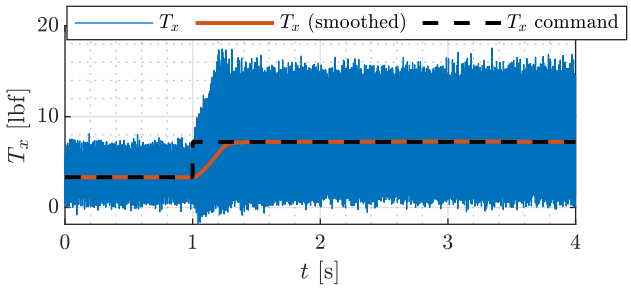

Fig. 8 Example data used for estimation of motor dynamics.

Flight dynamics modeling for propulsor dynamics is well-described by a lower-order representation of the dynamics, commonly in the form of a low pass filter. According to Ref. [44], time-dependent motor and ESC dynamics can be sufficiently modeled using first-order dynamics modeling the lag between a commanded and actual rotational speed. Expressed as a differential equation, this takes the form:

$$\dot{n} = \frac{1}{\tau}\left(n_{cmd} - n\right) \tag{27}$$

where n is the actual motor speed, n_{cmd} is the commanded motor speed, and τ is the time constant. However, for this work, the motor dynamics were found to be best described by second-order dynamics:

$$\ddot{n} + 2\zeta\omega_n\dot{n} + \omega_n^2 n = \omega_n^2 n_{cmd} \tag{28}$$

where ω_n is the natural frequency and ζ is the damping ratio. The second-order model was found to consistently provide lower output-error values and a superior visual model fit.

The motor dynamics appeared to be mostly independent of propeller rotation direction, airspeed, and incidence angle for the conditions tested. However, the dynamics did appear to significantly change if the motor rotational speed command was increasing or decreasing, with a speed increase having faster dynamics. Consequently, a model was

developed for positive and negative changes in propeller speed command. Table 3 shows the estimated parameters for the models in Eq. (27) and Eq. (28). The parameters are taken to be the average values identified from numerous different measurement time histories used for modeling.

Table 3 Estimated motor dynamics parameters for first-order and second-order models

Parameter	$\hat{\theta}$ for $+\Delta\eta$	$\hat{\theta}$ for $-\Delta\eta$
τ	0.127	0.188
ω_n	9.80	8.62
ζ	0.785	0.984

Model validation was performed through simulated reconstruction of measured data not used for model identification. Figure 9 shows the first-order and second-order model fits to measured data and the commanded signal. The results show that both models offer a sufficient fit to the data. The second-order model shows a closer fit, but the extra complexity of requiring an additional state for each motor in simulation may warrant implementation of the first-order model.

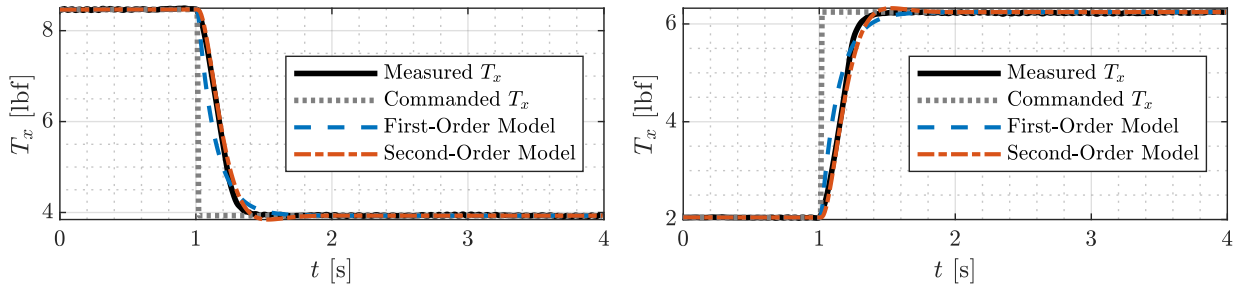

(a) Models for decreasing motor speed **(b) Models for increasing motor speed**

Fig. 9 Comparison of the modeled and measured response to motor step inputs.

VI. Propeller Aerodynamic Model Identification

This section develops the propeller aerodynamic modeling approach and presents sample modeling results. The propeller aerodynamic model relates propeller states to output forces and moments. At high incidence angles, all propeller force and moment components are expected to be significant, with the possible exception of side force, which was found to be negligible in other experiments [29, 30, 32].

A. Propeller Modeling Approach

As introduced previously in Sec. II, propeller aerodynamics in axial airflow can be described using advance ratio, propeller blade Reynolds number, and tip Mach number. Incidence angle becomes another factor for describing propeller aerodynamics at nonzero incidence. For the experimental propeller in this work, advance ratio and angle of incidence effects were expected to be the main contributing factors to the propeller aerodynamics. The propeller also operates

at low propeller blade Reynolds number (approximately 40,000 to 140,000), which was expected to be a smaller, but non-negligible factor. Since the testing was performed at subsonic propeller tip conditions, tip Mach number effects were neglected. Accordingly, the propeller aerodynamics for the current application were defined as a function of advance ratio J, incidence angle i_p, and propeller blade Reynolds number Re. The response variables were the dimensionless propeller force and moment coefficients, C_{T_x}, C_{T_y}, C_{T_z}, C_{Q_x}, C_{Q_y}, and C_{Q_z}, defined previously.

With factors describing propeller aerodynamics defined, a challenge becomes finding an adequate model structure to describe the complex aerodynamic phenomena in a form conducive to flight dynamic modeling and controller design. Interpolation of tabulated data is a common approach for storing propeller data, however, this provides little physical insight and can lead to practical problems in trimming and controller design due to disjointed, imperfect experimental data. Alternatively, polynomial models are a common choice for developing a mathematical description for simulation and controls applications due to their continuity and differentiability, as well as the physical insight gained from identified parameters. Polynomial models also facilitate modeling efficiency because data does not need to be acquired at every interior point (as is the case for tabulated data) and are more robust to measurement noise due to an inherent smoothing effect.

Use of polynomial aerodynamic models results in insightful, compact mathematical descriptions of complex phenomena analogous to a Taylor series expansion, but leads to the nontrivial task of developing a model structure which adequately captures the dominant aerodynamics while not over-parameterizing the model. Several different combinations of advance ratio, incidence angle, and propeller blade Reynolds number were explored as explanatory variables. The best choice of explanatory variables for high modeling accuracy and the fewest number of model terms was found to be normal advance ratio J_x, tangential advance ratio J_z, and propeller blade Reynolds number Re. The candidate model terms consisted of expansions of each explanatory variable up to cubic terms as well as all arrangements of cross terms up to a total of third order. Normal and tangential advance ratio are defined as

$$J_x = \frac{V \cos i_p}{nD} = J \cos i_p \tag{29}$$

$$J_z = \frac{V \sin i_p}{nD} = J \sin i_p \tag{30}$$

which follows a similar representation used for rotorcraft [18, 50]. This representation of advance ratio was also used in a previous propeller modeling effort which developed lookup tables for propulsive forces and moments for a quadrotor vehicle [48]. Propeller blade Reynolds number, defined in Eq. (4), was normalized and centered by 10^5,

$$\hat{Re} = \frac{Re - 10^5}{10^5} \tag{31}$$

to decorrelate its variation with the bias terms, avoid numerical problems in parameter estimation, and make the variable

align with the assumptions of a Taylor series expansion being around a reference point within the data set. J_x and J_z have reference values of zero and are not large in magnitude so their values can be directly used for model identification.

An overall challenge in developing a comprehensive propeller model for eVTOL aircraft is the highly nonlinear dependence of the propeller forces and moments on incidence angle i_p. Polynomial models describing a highly nonlinear dependence on certain variables result in sacrificing local modeling fit to optimize the fit for a global model. The global model also requires a large number of model terms to estimate. These difficulties were encountered when developing a global model covering the full test envelope. One potential remedy is to use polynomial splines [46], as was used in Sec V.A, however, this was complicated by a large number of possible spline knots coupled with little insight for their placement. Consequently, modeling focus shifted to developing multiple local models each covering a smaller range of propeller incidence angles. One explored approach was to develop a different model for each tested propeller incidence angle. This results in significantly fewer model terms to estimate for each model equation and a much better local model fit. However, this approach suffered from limited data at certain conditions and jaggedness between models at flight conditions near 90° of propeller incidence. Accordingly, the best approach was to develop a series of polynomial models each covering a limited range of incidence angles. In order to encourage pseudo-continuity between neighboring models, incidence angle region partitions were overlapped by up to 50% in each individual region. The ranges of incidence angles determined for aerodynamic model partitioning are shown in Fig. 10, which were selected manually in consultation with modeling statistics, data quality, and engineering insight. Optimal model partitioning strategies are an area of ongoing research that should be considered for future propeller modeling efforts [51].

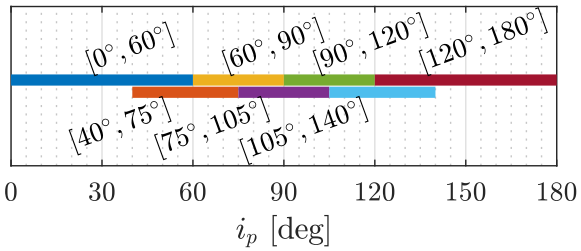

Fig. 10 Incidence angle partitions for propeller aerodynamic model development.

Additional considerations were needed to ensure the local models developed over each incidence angle interval were suitable for simulation implementation. Since the partitioned models all have a single point of convergence at zero airspeed, static data was included in the modeling data for each interval to encourage models to converge to similar values at zero airspeed. A static propeller model was also identified to deconflict small offsets between modeling regions at zero airspeed. Additionally, on the interval $0° \leq i_p \leq 60°$, it was required that the models be symmetric about $i_p = 0°$ to avoid discontinuities when crossing over this point. This is important because the model identification was performed on the interval $0° \leq i_p \leq 180°$, and due to axial symmetry, negative i_p values encountered in simulation will involve reflection

of the identified models over $i_p = 0°$. To force the modeling algorithm to capture this constraint, data used for modeling over $0° \leq i_p \leq 60°$ were duplicated and reflected over $i_p = 0°$ such that $C_{T_x}(-i_p) = C_{T_x}(+i_p)$, $-C_{T_y}(-i_p) = C_{T_y}(+i_p)$, $-C_{T_z}(-i_p) = C_{T_z}(+i_p)$, $C_{Q_x}(-i_p) = C_{Q_x}(+i_p)$, $-C_{Q_y}(-i_p) = C_{Q_y}(+i_p)$, and $-C_{Q_z}(-i_p) = C_{Q_z}(+i_p)$. This approach was effective at enforcing these constraints. Local model identification results will be shown next, followed by presentation of the approach used to blend local models and global modeling results.

B. Local Modeling Results

A propeller aerodynamic model structure and parameter estimates were identified using MOF modeling and least-squares parameter estimation for each partitioned i_p region described in the previous section. The modeling results for the clockwise propeller force and moment coefficients on the interval $0° \leq i_p \leq 60°$ are shown in Tables 4-5. The model parameters are presented in the order in which they were added to the model, so terms appearing first are most significant to the model. As an example of how the polynomial models would appear for usage, the clockwise rotating propeller model for C_{T_x} given in the first column of Table 4, is expressed in polynomial equation form as:

$$C_{T_x} = C_{T_{x_o}} + C_{T_{x_{J_x^2}}} J_x^2 + C_{T_{x_{J_z^2}}} J_z^2 + C_{T_{x_{\hat{Re}^3}}} \hat{Re}^3 + C_{T_{x_{J_x^3}}} J_x^3$$

The identified model structure and parameter estimates are different for each local model region and each propeller rotation direction.

Table 4 Clockwise propeller parameter estimates for C_{T_x}, C_{T_y}, and C_{T_z} models on $0° \leq i_p \leq 60°$

Term	$\hat{\theta} \pm s(\hat{\theta})$	Term	$\hat{\theta} \pm s(\hat{\theta})$	Term	$\hat{\theta} \pm s(\hat{\theta})$
$C_{T_{x_o}}$	$+1.17\times10^{-1} \pm 2.55\times10^{-4}$	$C_{T_{y_{J_z}}}$	$-6.79\times10^{-3} \pm 6.18\times10^{-4}$	$C_{T_{z_{J_z}}}$	$-1.97\times10^{-2} \pm 6.72\times10^{-4}$
$C_{T_{x_{J_x^2}}}$	$-2.88\times10^{-1} \pm 3.38\times10^{-3}$	$C_{T_{y_{J_x J_z}}}$	$+1.81\times10^{-2} \pm 2.52\times10^{-3}$	$C_{T_{z_{J_z^3}}}$	$-1.06\times10^{-2} \pm 4.77\times10^{-4}$
$C_{T_{x_{J_z^2}}}$	$+3.87\times10^{-2} \pm 5.06\times10^{-4}$	$C_{T_{y_{J_x^2 J_z}}}$	$+2.15\times10^{-3} \pm 2.56\times10^{-3}$	$C_{T_{z_{J_x J_z}}}$	$-1.96\times10^{-2} \pm 1.33\times10^{-3}$
$C_{T_{x_{\hat{Re}^3}}}$	$+5.89\times10^{-2} \pm 2.02\times10^{-3}$	$C_{T_{y_{J_z \hat{Re}^2}}}$	$+4.29\times10^{-4} \pm 1.17\times10^{-3}$		
$C_{T_{x_{J_x^3}}}$	$+9.17\times10^{-2} \pm 4.24\times10^{-3}$	$C_{T_{y_{J_z \hat{Re}}}}$	$-2.08\times10^{-2} \pm 1.07\times10^{-3}$		
		$C_{T_{y_{J_x J_z \hat{Re}}}}$	$+4.48\times10^{-2} \pm 2.64\times10^{-3}$		
		$C_{T_{y_{J_z^3}}}$	$+9.58\times10^{-4} \pm 2.41\times10^{-4}$		

The coefficient of determination R^2 for each identified model is shown in Table 6. As discussed previously, the R^2 metric reflects the amount of variation in the dependent variable about its mean value that is captured by the model. However, R^2 can be misleading because it always increases with addition of more model terms and is computed only from data used to fit the model, opposed to prediction data. Furthermore, the best R^2 value for a particular data set is dependent on output response signal-to-noise ratio [35]. Nonetheless, R^2 is used here to help interpret modeling results because the model structure determination strategy was configured to identify parsimonious models using both the PSE and R^2 metrics (see Sec. IV.B), and because of its familiarity to a broad audience.

Table 5 Clockwise propeller parameter estimates for C_{Q_x}, C_{Q_y}, and C_{Q_z} models on $0° \leq i_p \leq 60°$

Term	$\hat{\theta} \pm s(\hat{\theta})$	Term	$\hat{\theta} \pm s(\hat{\theta})$	Term	$\hat{\theta} \pm s(\hat{\theta})$
$C_{Q_{x_o}}$	$-7.73\times10^{-3} \pm 4.45\times10^{-5}$	$C_{Q_{y_{J_xJ_z}}}$	$-1.35\times10^{-2} \pm 9.39\times10^{-4}$	$C_{Q_{z_{J_z}}}$	$-1.56\times10^{-2} \pm 9.81\times10^{-4}$
$C_{Q_{x_{J_x^2}}}$	$+1.91\times10^{-2} \pm 2.68\times10^{-4}$	$C_{Q_{y_{J_xJ_z\hat{Re}}}}$	$-2.90\times10^{-2} \pm 2.82\times10^{-3}$	$C_{Q_{z_{J_xJ_z\hat{Re}}}}$	$-1.83\times10^{-2} \pm 2.99\times10^{-3}$
$C_{Q_{x_{J_xJ_z^2}}}$	$-4.68\times10^{-3} \pm 8.23\times10^{-5}$	$C_{Q_{y_{J_z}}}$	$+1.25\times10^{-2} \pm 4.68\times10^{-4}$	$C_{Q_{z_{J_x^2J_z}}}$	$-3.95\times10^{-2} \pm 3.99\times10^{-3}$
$C_{Q_{x_{J_x}}}$	$-5.96\times10^{-3} \pm 2.29\times10^{-4}$	$C_{Q_{y_{J_z^3}}}$	$-5.33\times10^{-3} \pm 3.13\times10^{-4}$	$C_{Q_{z_{J_z\hat{Re}}}}$	$+1.51\times10^{-2} \pm 1.51\times10^{-3}$
$C_{Q_{x_{J_x\hat{Re}}}}$	$-1.16\times10^{-3} \pm 1.15\times10^{-4}$	$C_{Q_{y_{J_z\hat{Re}}}}$	$+2.02\times10^{-2} \pm 1.12\times10^{-3}$	$C_{Q_{z_{J_xJ_z}}}$	$+3.08\times10^{-2} \pm 4.02\times10^{-3}$
		$C_{Q_{y_{J_z\hat{Re}^2}}}$	$-1.87\times10^{-2} \pm 1.50\times10^{-3}$		

Table 6 Coefficient of determination (R^2) for identified clockwise propeller aerodynamics models

i_p Region	C_{T_x}	C_{T_y}	C_{T_z}	C_{Q_x}	C_{Q_y}	C_{Q_z}
0°-60°	99.5	79.0	98.0	98.1	87.6	95.1
40°-75°	99.3	80.2	93.5	90.5	93.1	86.8
60°-90°	97.5	84.9	92.4	76.2	93.4	77.5
75°-105°	97.3	78.4	88.5	80.4	95.1	69.0
90°-120°	92.8	73.9	87.3	80.9	93.4	76.6
105°-140°	95.2	75.6	86.9	91.3	88.6	85.2
120°-180°	95.7	75.8	80.0	97.7	85.3	74.3
Static	78.4			42.8		

The R^2 values for axial thrust coefficient C_{T_x} indicate that its variation is well described over all incidence angles. The static C_{T_x} model (i.e. $J_x = J_z = 0$) has a lower value of R^2 because static thrust is well explained by the axial thrust coefficient mean value, and propeller blade Reynolds number has a less significant effect on modeling results than advance ratio. Axial torque coefficient C_{Q_x} is well modeled at most incidence angles, but is degraded closer to 90° incidence. A poor fit is observed for the C_{Q_x} static model, which can be explained by the same reasons as for the static C_{T_x} model. Normal force coefficient C_{T_z} is well identified from 0° to 90° incidence, with gradually decreasing model fit quality thereafter. Pitching moment coefficient C_{Q_y} has its best modeling fit near $i_p = 90°$, which is expected because this response is predicted to be minimal at low incidence angles [15] and occurs in tangential airflow due to differences in airflow through the front and rear facing portion of the propeller disk. Yawing moment coefficient C_{Q_z} has a good fit at low incidence, but degrades near and after $i_p = 90°$. Side force coefficient C_{T_y} has the lowest quality modeling results because this response is relatively small. However, the deterministic content was deemed large enough to be included as a modeled coefficient and its effect was confirmed in independent wind tunnel testing. Overall reduction of model quality near $i_p = 180°$ can be attributed to fewer modeling data points, sting interference, and highly complex aerodynamics associated with an approach to a vortex ring state [52]. Other regions where the modeling fit is lower quality can be attributed to low coefficient values (with consequent low signal-to-noise ratios) or highly nonlinear aerodynamic phenomena present for propeller operation over the large range of incidence angles and flight conditions.

While R^2 reflects model fit quality, comparison to validation data not used in the modeling process is generally considered a more reliable indicator of modeling success. Table 7 shows the percent NRMSE computed for each modeled response using modeling and validation data; Table 8 shows identical information for percent NMAE. Normalization is performed by the range of the measured response for all modeling data obtained for each coefficient to allow direct comparison between modeling and validation data as well as models defined on different ranges of incidence angles. The tabulated NRMSE and NMAE values for C_{T_x} and C_{Q_x} are the lowest and show similar values for both modeling and validation data indicating that a quality model has been identified. This is expected because axial aerodynamics have the biggest influence on propeller performance. NRMSE and NMAE values C_{T_z}, C_{Q_y}, and C_{Q_z} were slightly greater than the axial coefficients, but are still acceptably low and modeling values are comparable with validation values, providing confidence in the identified models. NRMSE and NMAE values for C_{T_y} are generally the highest among modeled responses, and there is a significant increase in error values for validation data compared to modeling data. This indicates that the models for C_{T_y} are lower quality than the remaining response variables, as expected, due to its small relative value compared to the other responses.

Table 7 Percent NRMSE for identified clockwise propeller aerodynamics models

(a) Modeling data

i_p Region	C_{T_x}	C_{T_y}	C_{T_z}	C_{Q_x}	C_{Q_y}	C_{Q_z}
0°-60°	0.87	2.44	1.83	1.25	2.75	2.38
40°-75°	0.70	4.13	3.61	1.93	3.80	4.60
60°-90°	0.69	5.20	4.50	2.71	4.75	7.57
75°-105°	0.65	6.33	5.06	3.05	3.62	9.19
90°-120°	1.51	6.46	4.25	3.66	3.23	7.93
105°-140°	1.65	5.79	3.22	3.15	3.20	5.69
120°-180°	2.63	4.90	2.61	2.61	3.72	4.87
Static	1.19			0.69		

(b) Validation data

i_p Region	C_{T_x}	C_{T_y}	C_{T_z}	C_{Q_x}	C_{Q_y}	C_{Q_z}
0°-60°	0.81	9.06	1.61	1.63	2.38	3.45
40°-75°	0.77	9.90	1.40	1.91	3.65	4.12
60°-90°	0.88	10.12	2.01	1.80	3.81	5.16
75°-105°	0.73	9.96	1.51	1.68	4.52	5.73
90°-120°	1.36	9.46	2.37	1.66	4.87	6.69
105°-140°	1.54	8.91	2.17	2.42	5.09	6.42
120°-180°	2.60	7.62	2.25	2.08	5.07	4.53
Static	1.20			1.47		

Table 8 Percent NMAE for identified clockwise propeller aerodynamics models

(a) Modeling data

i_p Region	C_{T_x}	C_{T_y}	C_{T_z}	C_{Q_x}	C_{Q_y}	C_{Q_z}
0°-60°	0.67	1.28	1.15	0.89	1.67	1.68
40°-75°	0.54	2.39	2.21	1.24	2.73	2.74
60°-90°	0.53	2.90	2.55	1.62	3.93	4.09
75°-105°	0.52	3.86	2.91	1.77	2.94	4.99
90°-120°	1.23	4.43	2.77	2.28	2.68	4.83
105°-140°	1.34	4.26	2.25	2.21	2.63	3.77
120°-180°	1.98	3.55	1.81	1.83	2.98	2.86
Static	0.92			0.55		

(b) Validation data

i_p Region	C_{T_x}	C_{T_y}	C_{T_z}	C_{Q_x}	C_{Q_y}	C_{Q_z}
0°-60°	0.67	5.65	1.10	1.19	1.82	2.67
40°-75°	0.61	6.53	1.04	1.25	3.07	3.19
60°-90°	0.73	6.98	1.48	1.15	3.26	4.37
75°-105°	0.63	7.59	1.25	1.34	3.72	4.84
90°-120°	1.19	7.36	1.83	1.29	3.96	5.72
105°-140°	1.27	6.96	1.74	2.00	4.00	5.23
120°-180°	2.06	5.94	1.90	1.59	3.96	3.23
Static	0.97			1.25		

C. Global Model Blending

Models identified over different ranges of certain variables require blending methods to eliminate discontinuities for simulation, where it is desirable to have continuous, differentiable, symmetric transition between modeling regions. Linear interpolation is simple and commonly used, but results in sharp corners at intersection points which makes simulation tasks, such as linearization or trimming, more challenging. Thus, an alternative approach was implemented for blending the identified propeller models partitioned by incidence angle. To illustrate the blending methodology used for this work, consider two partitioned polynomial models $C_1(x)$ and $C_2(x)$ which are used as components in a global model $C(x)$. The global model $C(x)$ is defined on the interval $x_1 \leq x \leq x_4$, the partitioned model $C_1(x)$ is defined on $x_1 \leq x \leq x_3$, and the partitioned model $C_2(x)$ defined on $x_2 \leq x \leq x_4$, where $x_1 < x_2 < x_3 < x_4$. The global function $C(x)$ will take on the value of $C_1(x)$ on $x_1 \leq x \leq x_2$ and $C_2(x)$ on $x_3 \leq x \leq x_4$, but the regions where the partitioned functions overlap will require a blended function $C_b(x)$. Thus, $C(x)$ is defined as:

$$C(x) = \begin{cases} C_1(x) & x_1 \leq x \leq x_2 \\ C_b(x) & x_2 < x < x_3 \\ C_2(x) & x_3 \leq x \leq x_4 \end{cases} \tag{32}$$

The approach taken to form $C_b(x)$ is using a quintic transition polynomial[¶] weighting function $f(\hat{x})$ that satisfies the boundary conditions $f(0) = 0$, $f'(0) = 0$, $f''(0) = 0$, $f(1) = 1$, $f'(1) = 0$, and $f''(1) = 0$ on the interval $0 \leq \hat{x} \leq 1$. Solving for the polynomial coefficients results in the weighting function:

$$f(\hat{x}) = 6\hat{x}^5 - 15\hat{x}^4 + 10\hat{x}^3 \tag{33}$$

To calculate the blended response $C_b(x)$ between two regions $C_1(x)$ and $C_2(x)$, the weights are

$$w_1(x) = f\left(\frac{x_3 - x}{x_3 - x_2}\right), \quad w_2(x) = 1 - w_1(x) \tag{34}$$

and the blended response is:

$$C_b(x) = w_1(x)C_1(x) + w_2(x)C_2(x) \tag{35}$$

The quintic polynomial weighting function values for the intervals described in the present example are plotted and compared to linear interpolation in Fig. 11.

Although there are many possible model blending methodologies in the literature, the transition polynomial approach was found to sufficiently blend the local propeller aerodynamic models. This approach creates a smooth global model

[¶]Credit: Daniel D. Moerder, NASA Langley Research Center

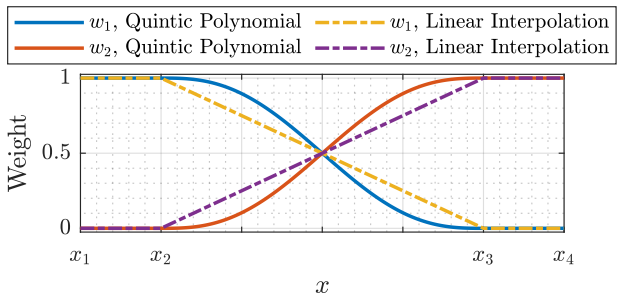

Fig. 11 Quintic polynomial weighting functions compared to linear interpolation weighting functions.

while allowing implementation simplicity for regions with non-uniform amounts of overlap. This approach would become less useful when more than two regions overlap or if partitioning is performed in multiple variables—in these cases, an alternative approach, such as Gaussian blending [53], would be more applicable.

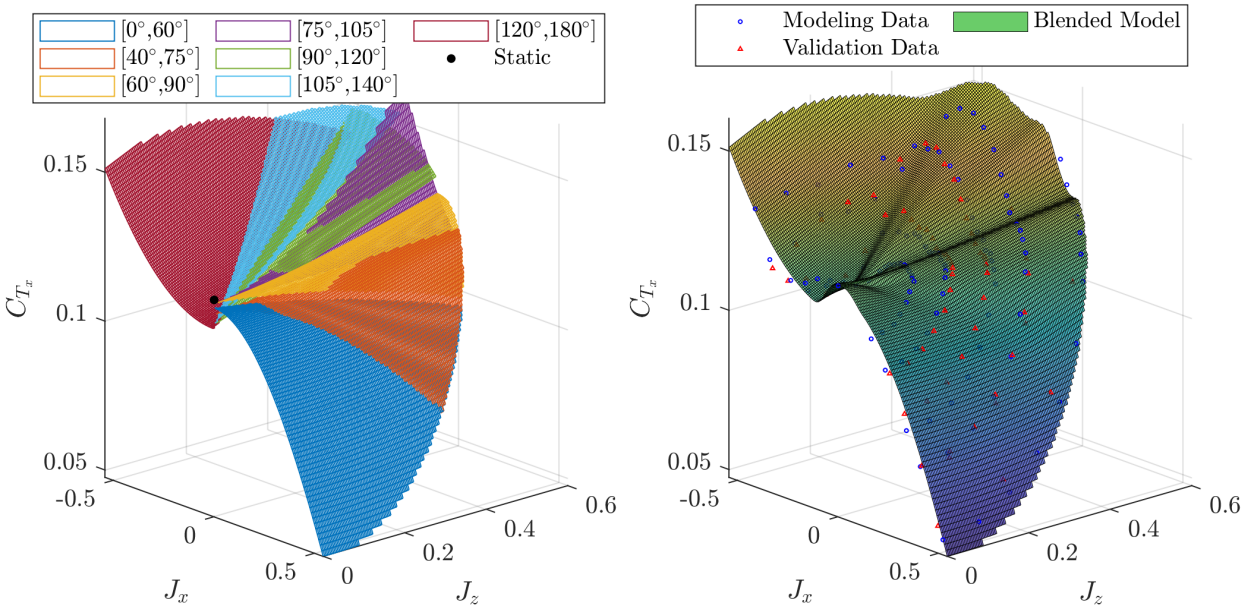

(a) Partitioned models over their regions of validity in i_p **(b) Global blended model compared to test data**

Fig. 12 Illustration of model blending methodology for C_{T_x} at a propeller blade Reynolds number of 100,000.

Figure 12 shows an example of the blending approach applied to the C_{T_x} model by plotting the response surface against J_x and J_z at a fixed propeller blade Reynolds number of 100,000. The individual local models, each identified over a different range of incidence angles, are shown in Fig. 12a. The global blended model response surface is shown in Fig. 12b where local models with overlapping incidence angles were blended using the quintic polynomial blending approach. After blending non-static models, additional blending was applied at low airspeed to incorporate the static model. Below the minimum nonzero freestream velocity tested of V_{min} = 14.5 ft/s, the response was blended with the

static model using the quintic polynomial function defined in Eq. (33), using the weights:

$$w_1(V) = f\left(\frac{V_{min} - V}{V_{min}}\right), \quad w_2(V) = 1 - w_1(V) \tag{36}$$

Figure 12b shows that the global response surface has a continuous and smooth surface globally, while also describing highly nonlinear aerodynamic phenomena over a large range of flight conditions. Modeling and validation test data with a propeller blade Reynolds number near 100,000 is also shown in the figure and is characterized well by the model. Small differences seen between the model and data are partially attributed to the Reynolds number for the displayed test data not perfectly matching the displayed model surface value.

D. Global Model Validation

The blended global model was validated following a similar methodology to local models. The percent NRMSE and NMAE computed for each global model response for both modeling and validation data is tabulated in Table 9. Global results reflect similar conclusions that were drawn from local models. C_{T_x} and C_{Q_x} models have the least normalized error followed by C_{T_z}, C_{Q_y}, and C_{Q_z}. Also, the error calculated using validation data is comparable to the modeling data indicating a quality model has been developed. C_{T_y} is observed to have the highest level of validation error, which is seen to be greater than the corresponding error metrics computed using modeling data, indicating a lower quality fit.

Table 9 Percent NRMSE and NMAE for the global clockwise propeller model

	C_{T_x}	C_{T_y}	C_{T_z}	C_{Q_x}	C_{Q_y}	C_{Q_z}
Modeling NRMSE	1.32	4.25	3.03	2.18	3.18	5.17
Validation NRMSE	1.23	7.88	4.18	1.73	3.98	5.16
Modeling NMAE	0.86	2.37	1.72	1.33	2.23	2.69
Validation NMAE	0.86	5.04	2.12	1.27	2.84	3.66

The individual normalized residuals $\hat{e}$ (see Eq. (24)) for both modeling and validation data are displayed as overlapping histograms in Fig. 13. The modeling and validation residuals are both zero-mean and appear to roughly follow a normal distribution with similar distribution statistics for C_{T_x}, C_{T_z}, C_{Q_x}, C_{Q_y}, and C_{Q_z}. The spread of validation residuals for C_{T_y} appears wider than for modeling residuals, which reflects previous observations suggesting that its modeled response is lower quality.

The local and global model fit and validation metrics show that the dominant responses have errors generally well below 5% and the weaker responses have errors generally less than 10%. This indicates that a high quality propeller aerodynamic model has been developed throughout the LA-8 flight envelope. However, the identified propeller aerodynamic models require specific implementation strategies for full-vehicle flight dynamics simulations. Methods for simulation integration are discussed next.

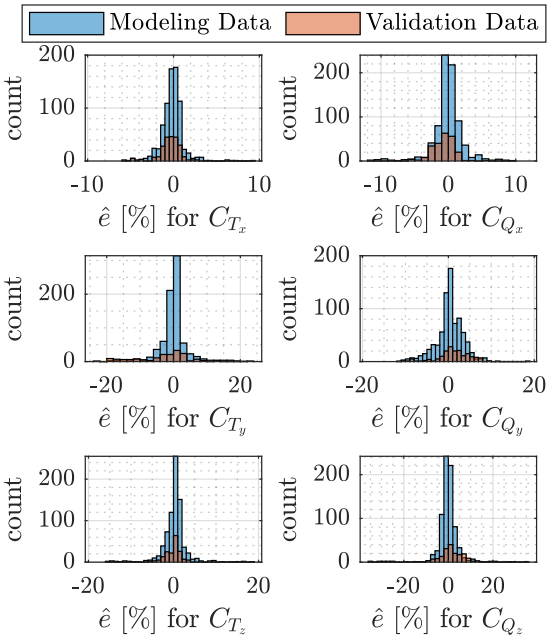

Fig. 13 Normalized residual histogram plots for the identified global model.

VII. Simulation Implementation

The identified propeller models detailed above were used for multiple high-fidelity tilt-wing aircraft simulations, so pertinent implementation considerations are briefly highlighted. This involves calculation of the local flow conditions at the propellers, computation of propeller incidence angle, transfer of propeller-generated forces and moments to a central location, and accounting for gyroscopic effects. This section considers the analysis for a single propeller, but these methods easily translate to systems with multiple propellers. All proceeding analysis assumes that the propeller is rigidly fixed to a tilting wing and that the propeller disk is perpendicular to airflow at zero vehicle angle of attack α, angle of sideslip β, and wing angle δ_w.

The airflow states in the fuselage body-axes at the vehicle center of gravity are described by the body-axis velocity components u, v, and w (or equivalently V, α, and β for nonzero flow velocity). These velocity components only describe the flow at the propellers at zero wing angle and zero angular velocity. Neglecting flow induced by the propeller, the relative velocity experienced by the propeller is generically also dependent on the propeller location relative to the center of gravity, $\Delta x = x_p - x_{cg}$, $\Delta y = y_p - y_{cg}$, and $\Delta z = z_p - z_{cg}$; the vehicle body-axis angular velocity components p, q, and r; and the wing rotation angle δ_w relative to the fuselage body-axes, defined as positive trailing edge down. Accounting for the offset in position is accomplished by following a similar procedure to airflow angle measurement position corrections [35, 54]. Next, velocity components are rotated into the propeller frame by a rotation in wing angle

δ_w. Thus, the velocity components at the propeller disk center are:

$$\begin{bmatrix} u_p \\ v_p \\ w_p \end{bmatrix} = \begin{bmatrix} \cos\delta_w & 0 & -\sin\delta_w \\ 0 & 1 & 0 \\ \sin\delta_w & 0 & \cos\delta_w \end{bmatrix} \begin{bmatrix} u + q\Delta z - r\Delta y \\ v + r\Delta x - p\Delta z \\ w + p\Delta y - q\Delta x \end{bmatrix} \tag{37}$$

The propeller incidence angle i_p is then computed from the local propeller velocity components:

$$i_p = \cos^{-1}\left(\frac{u_p}{\sqrt{u_p^2 + v_p^2 + w_p^2}}\right) \tag{38}$$

The incidence angle can be conceptualized as a combination of the local angle of attack and local angle of sideslip for the propeller, which determines the aerodynamic forces and moments due to assumed axial symmetry.

An additional flow angle must be defined to determine the direction of the auxiliary force and moment components T_y, T_z, Q_y, and Q_z. This quantity, defined here as ξ_p, is the angle specifying the local velocity projection onto the propeller disk plane, or the y_p–z_p plane. Figure 14 shows a schematic of the definition of ξ_p, which is calculated from the local propeller velocity:

$$\xi_p = \tan^{-1}\left(\frac{v_p}{w_p}\right) \tag{39}$$

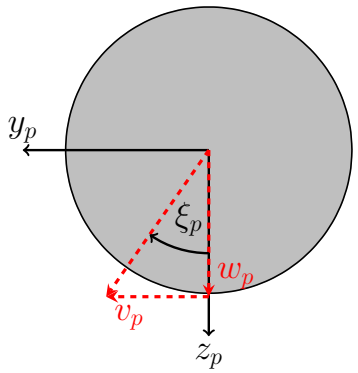

Fig. 14 Propeller disk schematic showing the definition of ξ_p in terms of the v_p and w_p.

The propeller-generated aerodynamic forces and moments are calculated using the polynomial models presented previously as a function of local advance ratio, propeller blade Reynolds number, and incidence angle. These forces and moments are expressed in the local propeller frame and must be transferred to the fuselage body frame to be combined with the airframe aerodynamics. This calculation includes a rotation by the angle ξ_p and then a subsequent rotation to

the fuselage body frame through the wing angle δ_w. The rotation matrix is:

$$\mathbf{R}^{bp} = \begin{bmatrix} \cos\delta_w & 0 & \sin\delta_w \\ 0 & 1 & 0 \\ -\sin\delta_w & 0 & \cos\delta_w \end{bmatrix} \begin{bmatrix} 1 & 0 & 0 \\ 0 & \cos\xi_p & \sin\xi_p \\ 0 & -\sin\xi_p & \cos\xi_p \end{bmatrix} \tag{40}$$

Let the local propeller-generated forces and moments be compactly notated as $\boldsymbol{T}^p = \begin{bmatrix} T_x & T_y & T_z \end{bmatrix}^T$ and $\boldsymbol{Q}^p = \begin{bmatrix} Q_x & Q_y & Q_z \end{bmatrix}^T$. The local propeller-generated forces and moments are then transferred to the fuselage body-axis force $\boldsymbol{T}^b$ and moment $\boldsymbol{Q}^b$ components at the center of gravity using:

$$\boldsymbol{T}^b = \mathbf{R}^{bp}\boldsymbol{T}^p \tag{41}$$

$$\boldsymbol{Q}^b = \mathbf{R}^{bp}\boldsymbol{Q}^p + \begin{bmatrix} \Delta x & \Delta y & \Delta z \end{bmatrix}^T \times \boldsymbol{T}^b \tag{42}$$

The forces and moments for all propellers are summed together to give the total propulsive force acting on the aircraft.

Another consideration for simulation is propulsor gyroscopic effects. The rotating portions of the propulsion system (electric motor components and the propeller) cause gyroscopic effects that influence aircraft dynamics when the propulsors are asymmetrically actuated or during a propulsor failure. While the aircraft equations of motion are generally used assuming a rigid body, gyroscopic effects can be incorporated by treating the gyroscopic terms as an external moment added to the standard equations of motion [35, 44]. The angular momentum of a single propulsor about its axis of rotation is $h_p = I_p\Omega_p$, where I_p is the moment of inertia of the rotating portion of the propulsor and Ω_p is the rotation rate in radians per second, with clockwise rotation being positive. The rotation rate $\Omega_p = 2\pi n$ is the output of the dynamic motor model described in Sec. V.B. For a propulsor mounted on a rotating wing, the angular momentum is rotated into the fuselage body-axis system by the wing angle δ_w, so the components of angular momentum in the body frame are:

$$\boldsymbol{h} = \begin{bmatrix} h_p\cos\delta_w & 0 & -h_p\sin\delta_w \end{bmatrix}^T \tag{43}$$

The gyroscopic moments $\boldsymbol{M}_g$ due to the propulsor angular momentum expressed in the body-axes are:

$$\boldsymbol{M}_g = \dot{\boldsymbol{h}} + \boldsymbol{\omega} \times \boldsymbol{h} \tag{44}$$

where $\boldsymbol{\omega} = \begin{bmatrix} p & q & r \end{bmatrix}^T$ in radians per second. Note that the transient torque required to increase or decrease the propeller rotational speed is modeled within the $\dot{\boldsymbol{h}}$ term in Eq. (44). The gyroscopic moments produced by each propulsor are then summed to calculate the net gyroscopic moments exerted on the vehicle.

VIII. Conclusions

This work developed and implemented an experimental approach for eVTOL vehicle propulsion model identification suitable for flight dynamics simulation. The identified models describe propulsion effects over a wide range of flight conditions seen in eVTOL vehicle flight, including propeller behavior at high incidence angles. The models consist of a static motor model, dynamic motor model, and propeller aerodynamics model, which are applied in series to relate input throttle commands to propeller-generated forces and moments. The static motor model computes commanded propeller speed as a function of PWM command and the normal component of freestream velocity at incidence angles below 90°. The dynamic motor model is composed of low-order dynamics equations relating commanded motor speed to actual motor speed. The propeller aerodynamics model computes the dimensionless force and moment coefficients from airflow and state variables. The aerodynamics were best described by several local models partitioned by incidence angle and expressed as a function of normal advance ratio, tangential advance ratio, and propeller blade Reynolds number. The novel propeller modeling approach utilized multivariate orthogonal function modeling to identity local polynomial models. Model blending strategies were presented to enable smooth, continuous description of aerodynamic phenomena across a wide flight envelope, and propeller-specific simulation implementation steps were outlined. Model validation indicated that the models are high quality and fit for the purpose of developing a high-fidelity model for the LA-8 aircraft. Because eVTOL vehicle dynamics are highly dependent on propulsive effects, accurate propulsion modeling is essential for high-fidelity simulator development. This paper proposed and demonstrated several novel propeller modeling techniques useful for modeling future eVTOL vehicles and provides progress in this new area of aerodynamic modeling research. Future eVTOL propulsion modeling studies are anticipated to further refine model development strategies.

Acknowledgments

This research was funded by the NASA Aeronautics Research Mission Directorate (ARMD) Transformational Tools and Technologies (TTT) project. Testing support was provided by David Hatke, Earl Harris, Ronald Busan, Sue Grafton, and Wes O'Neal. Photography support was provided by Lee Pollard. LA-8 vehicle support for propeller model development was provided by David North, Gregory Howland, Steven Geuther, and Robert McSwain. Conversations about this work with Eugene Morelli, John Foster, and many other colleagues at NASA Langley Research Center are acknowledged and greatly appreciated.

References

[1] Saeed, A. S., Younes, A. B., Cai, C., and Cai, G., "A survey of hybrid Unmanned Aerial Vehicles," *Progress in Aerospace Sciences*, Vol. 98, 2018, pp. 91–105. https://doi.org/10.1016/j.paerosci.2018.03.007.

[2] Silva, C., Johnson, W., Antcliff, K. R., and Patterson, M. D., "VTOL Urban Air Mobility Concept Vehicles for Technology

Development," *2018 Aviation Technology, Integration, and Operations Conference*, AIAA Paper 2018-3847, Jun. 2018. https://doi.org/10.2514/6.2018-3847.

[3] Antcliff, K. R., Whiteside, S. K. S., Kohlman, L. W., and Silva, C., "Baseline Assumptions and Future Research Areas for Urban Air Mobility Vehicles," *AIAA SciTech 2019 Forum*, AIAA Paper 2019-0528, Jan. 2019. https://doi.org/10.2514/6.2019-0528.

[4] Rothhaar, P. M., Murphy, P. C., Bacon, B. J., Gregory, I. M., Grauer, J. A., Busan, R. C., and Croom, M. A., "NASA Langley Distributed Propulsion VTOL Tilt-Wing Aircraft Testing, Modeling, Simulation, Control, and Flight Test Development," *14th AIAA Aviation Technology, Integration, and Operations Conference*, AIAA Paper 2014-2999, Jun. 2014. https://doi.org/10.2514/6.2014-2999.

[5] North, D. D., Howland, G., and Busan, R. C., "Design and Fabrication of the LA-8 Distributed Electric Propulsion VTOL Testbed," *AIAA SciTech 2021 Forum*, AIAA Paper 2021-1188, Jan. 2021. https://doi.org/10.2514/6.2021-1188.

[6] Geuther, S. C., and Fei, X., "LA-8 Computational Analysis and Validation Studies Using FlightStream," *AIAA SciTech 2021 Forum*, AIAA Paper 2021-1191, Jan. 2021. https://doi.org/10.2514/6.2021-1191.

[7] North, D. D., "Flight Testing of a Scale Urban Air Mobility Technology Testbed," *AIAA SciTech 2021 Forum*, AIAA Presentation, Jan. 2021. URL https://ntrs.nasa.gov/citations/20205010998, accessed March 2021.

[8] Simmons, B. M., and Murphy, P. C., "Wind Tunnel-Based Aerodynamic Model Identification for a Tilt-Wing, Distributed Electric Propulsion Aircraft," *AIAA SciTech 2021 Forum*, AIAA Paper 2021-1298, Jan. 2021. https://doi.org/10.2514/6.2021-1298.

[9] Busan, R. C., Murphy, P. C., Hatke, D. B., and Simmons, B. M., "Wind Tunnel Testing Techniques for a Tandem Tilt-Wing, Distributed Electric Propulsion VTOL Aircraft," *AIAA SciTech 2021 Forum*, AIAA Paper 2021-1189, Jan. 2021. https://doi.org/10.2514/6.2021-1189.

[10] Murphy, P. C., Simmons, B. M., Hatke, D. B., and Busan, R. C., "Rapid Aero Modeling for Urban Air Mobility Aircraft in Wind-Tunnel Tests," *AIAA SciTech 2021 Forum*, AIAA Paper 2021-1644, Jan. 2021. https://doi.org/10.2514/6.2021-1644.

[11] Geuther, S. C., North, D. D., and Busan, R. C., "Investigation of a Tandem Tilt-wing VTOL Aircraft in the NASA Langley 12-Foot Low-Speed Tunnel," NASA TM-2020-5003178, Jun. 2020.

[12] McSwain, R. G., Geuther, S. C., Howland, G., Patterson, M. D., Whiteside, S. K., and North, D. D., "An Experimental Approach to a Rapid Propulsion and Aeronautics Concepts Testbed," NASA TM-2020-220437, Jan. 2020.

[13] McCormick, B. W., *Aerodynamics, Aeronautics, and Flight Mechanics*, 2nd ed., John Wiley & Sons, New York, NY, 1995.

[14] Dommasch, D. O., *Elements of Propeller and Helicopter Aerodynamics*, Pitman Publishing Corporation, 1953.

[15] Phillips, W. F., *Mechanics of Flight*, 2nd ed., John Wiley & Sons, Hoboken, NJ, 2010.

[16] Greitzer, E. M., Spakovszky, Z. S., and Waitz, I. A., "Thermodynamics and Propulsion," *Lecture Notes, Massachusetts Institute of Technology*, 2006. URL http://web.mit.edu/16.unified/www/FALL/thermodynamics/notes/node86.html, accessed November 2020.

[17] Singleton, J. D., and Yeager, W. T., "Important Scaling Parameters for Testing Model-Scale Helicopter Rotors," *Journal of Aircraft*, Vol. 37, No. 3, 2000, pp. 396–402. https://doi.org/10.2514/2.2639.

[18] Leishman, J. G., *Principles of Helicopter Aerodynamics*, 2nd ed., Cambridge University Press, Cambridge, UK, 2016.

[19] Brandt, J., and Selig, M., "Propeller Performance Data at Low Reynolds Numbers," *49th AIAA Aerospace Sciences Meeting including the New Horizons Forum and Aerospace Exposition*, AIAA Paper 2011-1255, Jan. 2011. https://doi.org/10.2514/6.2011-1255.

[20] Deters, R. W., Ananda, G. K., and Selig, M. S., "Reynolds Number Effects on the Performance of Small-Scale Propellers," *32nd AIAA Applied Aerodynamics Conference*, AIAA Paper 2014-2151, Jun. 2014. https://doi.org/10.2514/6.2014-2151.

[21] Ribner, H. S., "Propellers in Yaw," NACA TR-820, 1945.

[22] Ribner, H. S., "Formulas for Propellers in Yaw and Charts of the Side-Force Derivative," NACA TR-819, 1945.

[23] Crigler, J. L., and Gilman Jr., J., "Calculation of Aerodynamic Forces on a Propeller in Pitch or Yaw," NACA TN-2585, Jan. 1952.

[24] De Young, J., "Propeller at High Incidence," *Journal of Aircraft*, Vol. 2, No. 3, 1965, pp. 241–250. https://doi.org/10.2514/3.43646.

[25] Smith, H. R., "Engineering Models of Aircraft Propellers at Incidence," Ph.D. thesis, University of Glasgow, Jan. 2015.

[26] McCormick, B. W., Aljabri, A. S., Jumper, S. J., and Martinovic, Z. N., "The Analysis of Propellers Including Interaction Effects," NASA CR-158111, 1979.

[27] Theys, B., Dimitriadis, G., Hendrick, P., and De Schutter, J., "Experimental and Numerical Study of Micro-Aerial-Vehicle Propeller Performance in Oblique Flow," *Journal of Aircraft*, Vol. 54, No. 3, 2017, pp. 1076–1084. https://doi.org/10.2514/1.C033618.

[28] Leng, Y., Yoo, H., Jardin, T., Bronz, M., and Moschetta, J.-M., "Aerodynamic Modeling of Propeller Forces and Moments at High Angle of Incidence," *AIAA SciTech 2019 Forum*, AIAA Paper 2019-1332, Jan. 2019. https://doi.org/10.2514/6.2019-1332.

[29] McLemore, H. C., and Cannon, M. D., "Aerodynamic Investigation of a Four-Blade Propeller Operating through an Angle-of-Attack Range from 0° to 180°," NACA TN-3228, Jun. 1954.

[30] Yaggy, P. F., and Rogallo, V. L., "A Wind-Tunnel Investigation of Three Propellers Through an Angle-of-Attack Range from 0° to 85°," NASA TN D-318, May 1960.

[31] Kuhn, R. E., and Draper, J. W., "Investigation of the Aerodynamic Characteristics of a Model Wing-Propeller Combination and of the Wing and Propeller Separately at Angles of Attack up to 90°," NACA TR-1263, 1956.

[32] Theys, B., Dimitriadis, G., Andrianne, T., Hendrick, P., and De Schutter, J., "Wind Tunnel Testing of a VTOL MAV Propeller in Tilted Operating Mode," *2014 International Conference on Unmanned Aircraft Systems (ICUAS)*, May 2014, pp. 1064–1072. https://doi.org/10.1109/ICUAS.2014.6842358.

[33] Leng, Y., Jardin, T., Bronz, M., and Moschetta, J.-M., "Experimental Analysis of Propeller Forces and Moments at High Angle of Incidence," *AIAA SciTech 2019 Forum*, AIAA Paper 2019-1331, Jan. 2019. https://doi.org/10.2514/6.2019-1331.

[34] Simmons, B. M., and Hatke, D. B., "Investigation of High Incidence Angle Propeller Aerodynamics for Subscale eVTOL Aircraft," NASA TM, 2021. To be published.

[35] Morelli, E. A., and Klein, V., *Aircraft System Identification: Theory and Practice*, 2nd ed., Sunflyte Enterprises, Williamsburg, VA, 2016.

[36] Morelli, E. A., "Global Nonlinear Aerodynamic Modeling Using Multivariate Orthogonal Functions," *Journal of Aircraft*, Vol. 32, No. 2, 1995, pp. 270–277. https://doi.org/10.2514/3.46712.

[37] Morelli, E. A., and DeLoach, R., "Wind Tunnel Database Development Using Modern Experiment Design and Multivariate Orthogonal Functions," *41st Aerospace Sciences Meeting and Exhibit*, AIAA Paper 2003-653, Jan. 2003. https://doi.org/10.2514/6.2003-653.

[38] Morelli, E. A., and DeLoach, R., "Response Surface Modeling using Multivariate Orthogonal Functions," *39th AIAA Aerospace Sciences Meeting and Exhibit*, AIAA Paper 2001-0168, Jan. 2001. https://doi.org/10.2514/6.2001-168.

[39] Barron, A. R., "Predicted Squared Error: A Criterion for Automatic Model Selection," *Self-Organizing Methods in Modeling*, Farlow, S. J., Ed., Marcel Dekker, Inc., New York, NY, 1984, pp. 87–104.

[40] Morelli, E. A., "Real-Time Global Nonlinear Aerodynamic Modeling for Learn-To-Fly," *AIAA Atmospheric Flight Mechanics Conference*, AIAA Paper 2016-2010, Jan. 2016. https://doi.org/10.2514/6.2016-2010.

[41] Morelli, E. A., "Practical Aspects of Real-Time Modeling for the Learn-To-Fly Concept," *2018 Atmospheric Flight Mechanics Conference*, AIAA Paper 2018-3309, Jun. 2018. https://doi.org/10.2514/6.2018-3309.

[42] Jategaonkar, R. V., *Flight Vehicle System Identification: A Time-Domain Methodology*, 2nd ed., American Institute of Aeronautics and Astronautics, Reston, VA, 2015. https://doi.org/10.2514/4.102790.

[43] Chai, T., and Draxler, R. R., "Root mean square error (RMSE) or mean absolute error (MAE)? – Arguments against avoiding RMSE in the literature," *Geoscientific Model Development*, Vol. 7, No. 3, 2014, pp. 1247–1250. https://doi.org/10.5194/gmd-7-1247-2014.

[44] Stevens, B. L., Lewis, F. L., and Johnson, E. N., *Aircraft Control and Simulation: Dynamics, Controls Design, and Autonomous Systems*, 3rd ed., John Wiley & Sons, Hoboken, New Jersey, 2015.

[45] Gundlach, J., *Designing Unmanned Aircraft Systems: A Comprehensive Approach*, Reston ,VA, 2012. https://doi.org/10.2514/4.868443.

[46] Morelli, E. A., "Efficient Global Aerodynamic Modeling from Flight Data," *50th AIAA Aerospace Sciences Meeting including the New Horizons Forum and Aerospace Exposition*, AIAA Paper 2012-1050, Jan. 2012. https://doi.org/10.2514/6.2012-1050.

[47] Morelli, E. A., "Estimating Noise Characteristics from Flight Test Data using Optimal Fourier Smoothing," *Journal of Aircraft*, Vol. 32, No. 4, 1995, pp. 689–695. https://doi.org/10.2514/3.46778.

[48] Foster, J. V., and Hartman, D., "High-Fidelity Multi-Rotor Unmanned Aircraft System (UAS) Simulation Development for Trajectory Prediction Under Off-Nominal Flight Dynamics," *17th AIAA Aviation Technology, Integration, and Operations Conference*, AIAA Paper 2017-3271, Jun. 2017. https://doi.org/10.2514/6.2017-3271.

[49] Russell, C., Jung, J., Willink, G., and Glasner, B., "Wind Tunnel and Hover Performance Test Results for Multicopter UAS Vehicles," *American Helicopter Society 72nd Annual Forum*, West Palm Beach, FL, May 2016.

[50] Johnson, W., *Rotorcraft Aeromechanics*, Cambridge University Press, 2013.

[51] Weinstein, R., and Hubbard, J. E., "Global Aerodynamic Modeling Using Automated Local Model Networks in Real Time," *AIAA SciTech 2020 Forum*, AIAA Paper 2020-0762, Jan. 2020. https://doi.org/10.2514/6.2020-0762.

[52] Johnson, W., "Model for Vortex Ring State Influence on Rotorcraft Flight Dynamics," NASA TP-2005-213477, Dec. 2005.

[53] Morelli, E., and Ward, D., "Automated Simulation Updates Based on Flight Data," *AIAA Atmospheric Flight Mechanics Conference and Exhibit*, AIAA Paper 2007-6714, Aug. 2007. https://doi.org/10.2514/6.2007-6714.

[54] Grauer, J. A., "Position Corrections for Airspeed and Flow Angle Measurements on Fixed-Wing Aircraft," NASA TM-2017-219795, Nov. 2017.